Journal of Applied Computational Intelligence

eISSN: 1234-5678

Vol. 4, No. 1, January, 2026

UniFormerV2 Model for Robotic Deburring Force Control Oriented to Six-Dimensional Force and Surface Profile Data Streams

Waldemar Brzozowski[1,*], Bronisław Kaczor[1], Arkadiusz Sadowski[1]

[1] *Faculty of Electrical Engineering, Warsaw University of Technology, Warsaw, 00-661, Poland*

Received 13 October 2025; Revised 26 December 2025; Accepted 09 January 2026; Published 17 January 2026

Abstract

Robotic deburring remains difficult when burr geometry, local stiffness, and tool contact conditions change faster than a conventional force controller can interpret them. This paper proposes a UniFormerV2-based force-control model that fuses six-dimensional wrist force signals with streaming surface profile features for adaptive deburring of machined aluminum alloy edges. The method constructs synchronized force-profile tokens from heterogeneous sensor streams, separates short contact impulses from longer surface-trend cues, and predicts a bounded normal-force compensation command for an admittance-controlled spindle end-effector. To improve deployability in industrial finishing cells, the model includes confidence-weighted fusion and latency-aware inference so that surface look-ahead can be reduced when profile measurements become unreliable. Experiments were conducted on 420 edge segments covering straight, convex, concave, and interrupted burrs, with six feed speeds and four nominal contact-force levels. Compared with PID admittance control, LSTM fusion, and a compact Transformer baseline, the proposed model reduced normal-force RMSE to 1.18 N, improved burr removal rate to 96.4%, lowered post-process Ra to 0.81 micrometer, and decreased force overshoot by 37.8% under profile discontinuity. The inference latency was 8.7 ms on an industrial GPU and remained below the 20 ms control-cycle limit. These results indicate that coupled force and surface streams provide a practical basis for learning contact-sensitive control policies without sacrificing the interpretability required in robotic finishing cells.

Keywords: Robotic Deburring; Six-Dimensional Force Sensing; Surface Profile Stream; UniFormerV2; Adaptive Force Control

1. Introduction

Robotic deburring has moved from a peripheral automation task to a quality-critical operation in aerospace, automotive, die-casting, and precision equipment manufacturing, where edge integrity affects fatigue resistance, assembly tolerance, sealing reliability, and downstream inspection yield [1]. Unlike free-space machining, deburring is dominated by intermittent contact between a rotating tool and a small, irregular material ridge whose height, root thickness, and local support stiffness can vary within a few millimeters [2]. Manual operators compensate for those variations by listening to spindle load, feeling vibration, and visually judging the residual ridge, yet industrial robots normally receive only position programs and a limited force signal [3]. The mismatch between geometric uncertainty and programmed motion produces under-cut burr roots, local gouging, thermal discoloration, and unstable tool wear [4]. Six-dimensional force-torque sensors have improved the observability of contact state because tangential forces, normal forces, and moment components provide indirect evidence of tool engagement and edge constraint [5]. However, force

* Corresponding author: waldemar.br@pw.edu.pl

https://doi.org/10.68406/jaci.2026.vol4iss1no3:28-41

➢ This is an open access article under the CC BY-NC-SA 4.0 license (https://creativecommons.org/licenses/by/4.0/).

© Authors retain all copyrights.

data alone cannot distinguish a tall flexible burr from a shallow but hard-supported corner when both generate similar transient peaks [6].

Surface profile acquisition offers a complementary route for deburring because structured light, laser triangulation, and compact depth cameras can describe edge height, residual ridge width, chamfer continuity, and waviness before or during tool engagement [7]. In practice, the profile stream is noisy, partially occluded by chips or coolant, and sampled at a rate different from the force-torque sensor [8]. Classical force control methods, including impedance, admittance, and hybrid position-force strategies, are effective when the desired contact model is known and slowly varying [9]. Their performance decreases when the surface profile changes abruptly or when burr stiffness evolves during cutting, because a fixed gain cannot simultaneously suppress impact and maintain sufficient material removal [10]. Data-driven controllers have been introduced to learn nonlinear mappings between sensing and force correction, but recurrent models often smooth out sharp contact events, while standard Transformers can be costly for short-cycle industrial control [11]. A controller for deburring therefore needs a representation that preserves local force impulses, tracks longer surface morphology, and remains computationally compatible with a millisecond-level control loop [12].

This study develops a UniFormerV2 model for robotic deburring force control oriented to synchronized six-dimensional force and surface profile data streams. The central idea is to treat force-torque measurements and profile descriptors as two coupled streams rather than as independent monitoring channels. The contribution is organized around three technical elements: synchronized force-profile token construction, dual-stream UniFormerV2 fusion for contact-state representation, and bounded normal-force compensation embedded in an admittance controller. A local token mixer captures high-frequency force disturbances, while profile-aware global relation modeling captures the slower geometric trend of burr height, root width, curvature, and discontinuity. The model is trained on experimentally collected edge segments and is evaluated against conventional and learning-based baselines using force tracking, removal quality, robustness, and inference latency.

To make the argument traceable from sensing requirements to process evidence, the remainder of this paper is organized around the progression from background, to model design, to experimental verification. Section 2 reviews robotic deburring force control, multimodal sensing, and transformer-based temporal modeling for industrial manipulation. Section 3 presents the dual-stream sensing architecture, the UniFormerV2 force-control formulation, and the training objective used for contact-sensitive command compensation. Section 4 describes the experimental platform, datasets, evaluation metrics, and comparative results using nine planned figures and one quantitative table. Section 5 concludes the paper by identifying the main contribution, current limitations, and future research directions.

2. Related Work

2.1. Robotic Deburring Force Control

Chang et al. [13] investigated position-adaptive impedance control for curved-mold polishing, which provides a representative example of adaptive force regulation rather than a complete solution to highly variable deburring edges. Comparable scheduling decisions often remain coarse relative to the local geometry of a burr. These systems are robust for repeatable castings but become inefficient when burr morphology changes across batches or when a machined contour contains local interruptions [14]. Active force control introduced a more flexible mechanism by regulating the normal interaction force between tool and workpiece, with impedance control shaping the apparent mechanical response and admittance control converting measured forces into corrective motion [15]. Hybrid position-force control further separates constrained and unconstrained directions, but its effectiveness depends on knowing which direction should be force controlled at each instant [16].

Several adaptive and learning-assisted strategies have been proposed to address this limitation. Gain scheduling can adjust admittance parameters according to measured force magnitude or estimated material class, but its decision variables often remain coarse relative to the local geometry of a burr. Model predictive force control can enforce actuator limits and surface-quality constraints, although it requires a sufficiently accurate process model and may be sensitive to online identification errors. Reinforcement learning offers a way to discover nonlinear control policies, yet exploration in contact-rich finishing is costly because tool breakage and workpiece damage cannot be treated as ordinary training samples [17]. Supervised imitation from expert trajectories is safer, but the learned policy may reproduce operator bias and may fail when sensing conditions differ from demonstrations [18]. These observations motivate a controller that preserves the transparency of admittance regulation while using learned representations to estimate when and how the force command should be corrected.

2.2. Multimodal Sensing and Transformer Models

Force-torque sensing has been widely used for contact classification, slip detection, surface following, and tool-condition monitoring because the six components contain coupled information about normal pressure, tangential resistance, and moment balance [19]. Surface profile sensing supplies a different form of evidence by describing the

geometry that will be encountered by the tool, including burr height, edge radius, root width, and local discontinuity [20]. Fusion of these modalities is attractive because force signals represent what is happening at the contact interface, while profile signals describe why that contact state is likely to occur [21]. Conventional fusion methods concatenate handcrafted features or align the modalities through Kalman filtering, but they often assume synchronous sampling and stable feature distributions [22]. In deburring, these assumptions are frequently violated by vibration, chip occlusion, calibration drift, and tool wear [23].

Transformer architectures have improved sequence modeling by learning long-range dependencies through attention, yet their direct use in industrial force control is limited by computational cost and the risk of ignoring sharp local events. Lightweight temporal Transformers reduce latency, but many of them still treat all tokens with similar global operations, which can dilute short force impulses that carry contact-state information. UniFormer-style architectures combine convolution-like local aggregation with attention-like global relation modeling, making them relevant for signal streams that contain both abrupt and slowly varying phenomena. UniFormerV2 extends this idea with efficient token mixing and hierarchical representation, which is suitable for a force-profile stream where local peaks, edge curvature, and path-level process context coexist. The research gap addressed here is the lack of a deburring controller that explicitly couples six-dimensional force dynamics with surface profile morphology in a UniFormerV2 framework while reporting control accuracy, surface quality, removal effectiveness, and cycle-level latency under varied burr conditions.

3. Dual-Stream UniFormerV2 Force-Control Method

3.1. Sensing and Synchronization Architecture

The proposed system uses an industrial six-axis robot, a high-speed spindle, a compliant deburring tool, a wrist-mounted six-dimensional force-torque sensor, and an inline surface-profile sensor positioned ahead of the tool center point. The 38 mm look-ahead offset is converted into a time horizon according to feed speed, allowing the controller to observe geometric discontinuities before the tool reaches them. The force stream contains three forces and three moments sampled at 1 kHz. The profile stream is resampled from the laser line measurement and describes local burr height, root width, curvature, gradient, roughness proxy, and discontinuity score. Figure 1 illustrates how the two streams are acquired, synchronized, encoded, and used for bounded force compensation before the admittance controller updates the robot motion.

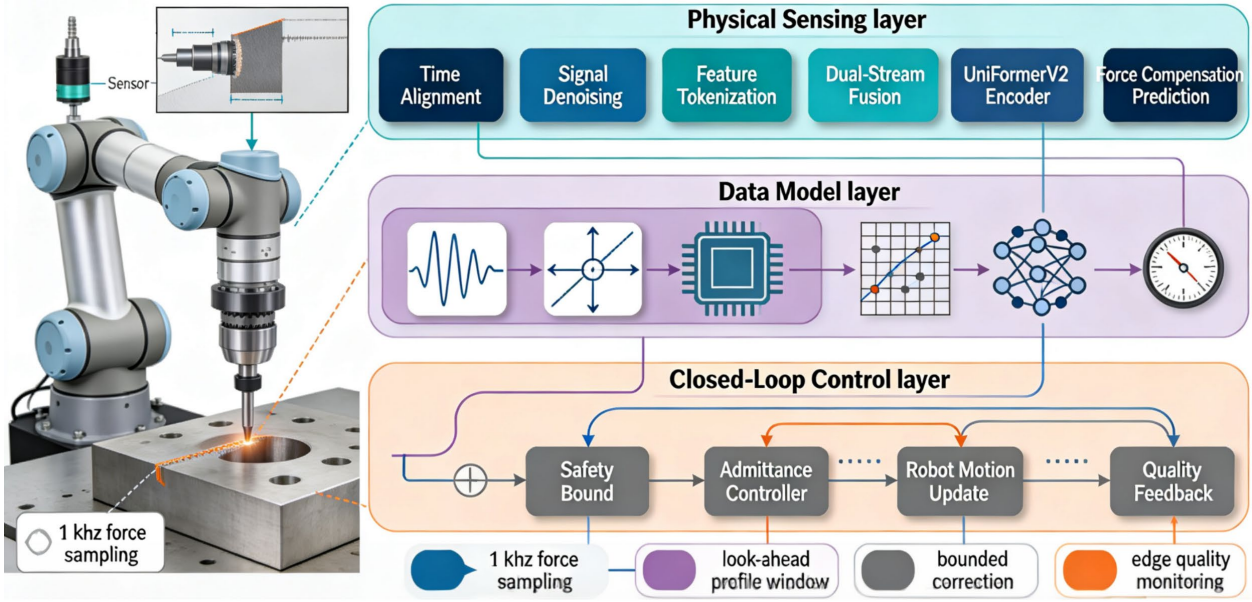


Figure 1. Placeholder for the dual-stream robotic deburring force-control workflow

The two streams are aligned through a sliding control window centered on the current tool pose. Force samples are filtered with a low-delay Savitzky-Golay smoother and transformed from the sensor frame to the tool frame. Surface profile descriptors are interpolated along the planned edge coordinate and assigned to the nearest force window according to robot encoder timestamps. This alignment avoids assuming that the profile sensor and the force sensor share the same native sampling rate. It also permits the model to observe a short segment of upcoming geometry while retaining the measured contact history behind the tool.

A separate calibration routine defines the relation between the laser profile coordinate, robot base frame, and instantaneous tool frame. The edge coordinate is computed from the nominal path, but local surface normals are updated from the profile stream so that normal-force regulation does not rely only on the offline CAD model. The six moment

channels are retained because deburring often creates a lever-arm effect when the tool engages the burr root away from the nominal contact center. In preliminary inspection, the moment about the tool tangent changed earlier than the normal force when the tool approached an interrupted edge, which is why the model receives the full wrench rather than a reduced scalar force.

$$x_t = \left[F_x, F_y, F_z, M_x, M_y, M_z\right]_t, p_t = \left[h_b, w_b, \kappa, g_p, r_p, d_p\right]_t \quad (1)$$

The expression defines the synchronized force vector and profile descriptor vector at time step t, where h_b is burr height, w_b is root width, κ is edge curvature, g_p is the profile gradient, r_p is a roughness proxy, and d_p is the discontinuity score. These variables are deliberately kept low dimensional because the objective is real-time force regulation rather than offline surface reconstruction.

The synchronization window is designed for online use. Each window contains enough force history to observe impact decay and enough profile look-ahead to recognize a discontinuity before the tool reaches it. A confidence value is attached to every profile descriptor. Low confidence is produced when reflected intensity saturates, when the laser stripe is partially hidden by chips, or when the profile fit has a residual error above the calibrated limit. Instead of discarding those samples, the fusion block receives the confidence value through the profile embedding. This treatment prevents the controller from treating missing geometry as a flat and reliable surface.

3.2. UniFormerV2 Fusion and Force Command Compensation

For each control window, the force tensor and profile tensor are projected into tokens with separate linear embeddings. The force branch emphasizes short-window local mixing so that impact peaks, burr fracture events, and spindle runout are not smoothed away, whereas the profile branch uses wider contextual mixing to preserve slower geometric tendencies along the edge. The profile branch uses a wider contextual mixer because burr height and edge curvature change more slowly than contact impulses but still affect the future normal-force demand. Cross-stream fusion is then performed so that force events can be interpreted in relation to the upcoming surface geometry rather than as isolated peaks.

$$z_t = U_\theta\left(E_f(x_{t-L:t}), E_p(p_{t-L:t+H})\right) \quad (2)$$

The UniFormerV2 encoder U_θ receives a backward-looking force window and a slightly forward-looking profile window. The horizon H represents the profile look-ahead distance converted into time through the current feed speed. The encoder output z_t is used to predict a bounded force correction rather than a full robot motion command.

$$f_n^*(t) = clip(f_r(t) + \Delta f_\theta(z_t), f_{min}, f_{max}) \quad (3)$$

The compensated normal-force command $f_n^*(t)$ is injected into the admittance layer. The clipping operation enforces process limits and prevents the learned component from producing commands outside the validated force envelope.

The model is deliberately smaller than a general video transformer. The contact window is short, the profile descriptors are structured, and the output space is a bounded force correction. The UniFormerV2 blocks are therefore arranged in two stages: an early stage emphasizes local mixing over neighboring force samples, and a later stage uses global relations to connect force events with the incoming profile. This division reduces attention cost and keeps the inductive bias close to the mechanics of deburring. Local blocks respond to impulsive tool contact; global blocks interpret whether the impulse is expected from geometry or represents a control error.

The output layer estimates the correction in the normal direction and two auxiliary confidence scores. The first score indicates whether the correction is driven primarily by force history or profile look-ahead. The second score indicates whether the current state is inside the training distribution. During deployment, these scores modulate branch weighting and provide an engineering check on whether the learned correction should be trusted under occlusion, reflectance loss, or unusual force transients. These scores are not used as additional performance indicators but as interpretability signals for process engineers who need to understand why the controller changes the force command.

3.3. Training Protocol and Deployment Logic

Training samples are built from synchronized edge segments collected under controlled variation of burr geometry, feed speed, spindle speed, tool angle, and nominal contact force. The label for each segment is derived from a calibrated reference pass and post-process measurement, not from a single operator judgment. During deployment, the model runs in the outer loop at 50 Hz, while the inner robot controller maintains the standard servo cycle. Figure 2 is placed in this section to describe the model architecture and its connection to the admittance controller.

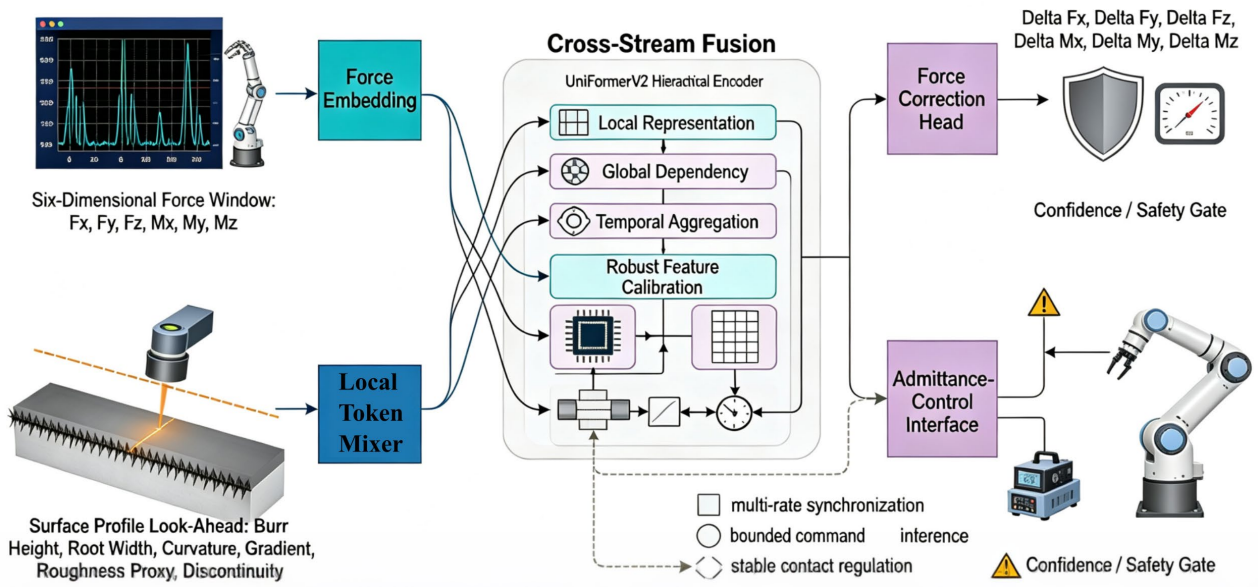


Figure 2. Placeholder for the UniFormerV2 dual-stream fusion architecture and bounded admittance-control interface

The deployment logic is intentionally conservative. If profile confidence falls below a threshold because of occlusion or reflective noise, the controller reduces the profile branch weight and relies more strongly on force history. If the measured force exceeds the safety threshold, the learned correction is bypassed and the admittance layer retracts the tool along the local normal. This design keeps the learned model inside a supervisory structure that is compatible with industrial acceptance testing.

The dataset is divided by physical edge segment rather than by overlapping window, so that neighboring windows from the same burr do not appear in both training and testing sets. The split contains 70% training segments, 15% validation segments, and 15% test segments. Segment-level splitting is important for a deburring process because adjacent windows from the same edge share nearly identical geometry and would otherwise overstate generalization.

$$L = \lambda_1 \left\| f_n^* - f_n^{ref} \right\|_1 + \lambda_2 \|\Delta v_t\|_2^2 + \lambda_3 max\left(0, R_a - R_a^{lim}\right) \quad (4)$$

The training objective combines reference-force tracking, velocity smoothness, and a surface-quality penalty. The tracking term has the largest weight, the smoothness term suppresses abrupt command changes, and the surface-quality term is activated when the labeled segment exceeds the roughness limit. The last term is activated only when the predicted control behavior is associated with roughness above the process limit in the labeled segment.

During online control, the robot executes the nominal path from the manufacturing program, while the admittance layer modifies the small normal displacement needed to realize the compensated force command. Tangential motion remains path dominated because uncontrolled tangential deviation could change the edge radius. The controller logs every force correction, confidence value, and safety gate activation. These logs are used after each trial to connect process outcomes with specific sensing events, which is essential for a model that will be judged not only by prediction error but also by the traceability of its actions in a production cell.

4. Experimental Evaluation and Data Analysis

4.1. Experimental Setup and Dataset

The experimental platform used a 20 kg payload industrial robot, a 12,000-rpm electric spindle, a carbide rotary file, a six-dimensional wrist sensor with 0.05 N force resolution, and a laser profile head mounted 38 mm ahead of the tool contact point. Aluminum 6061-T6 and cast aluminum samples were prepared with four edge categories: straight, convex, concave, and interrupted. Both materials appeared in each edge category, and repeated trials were distributed to avoid training the model on only one material-condition combination. Each category contained burr heights from 0.18 to 1.25 mm and root widths from 0.12 to 0.74 mm. The full dataset contained 420 usable edge segments after removing runs affected by sensor saturation or severe chip adhesion. Segment-level partitioning is recommended for contact-rich robotic datasets because adjacent time windows from the same physical edge can otherwise leak process information into the test set [24]. Figure 3(a) shows the number of usable segments in the four edge categories, with 126 straight, 102 convex, 96 concave, and 96 interrupted segments. Figure 3(b) maps burr height against root width and shows that difficult samples were concentrated in the high-height, wide-root region rather than being distributed uniformly.

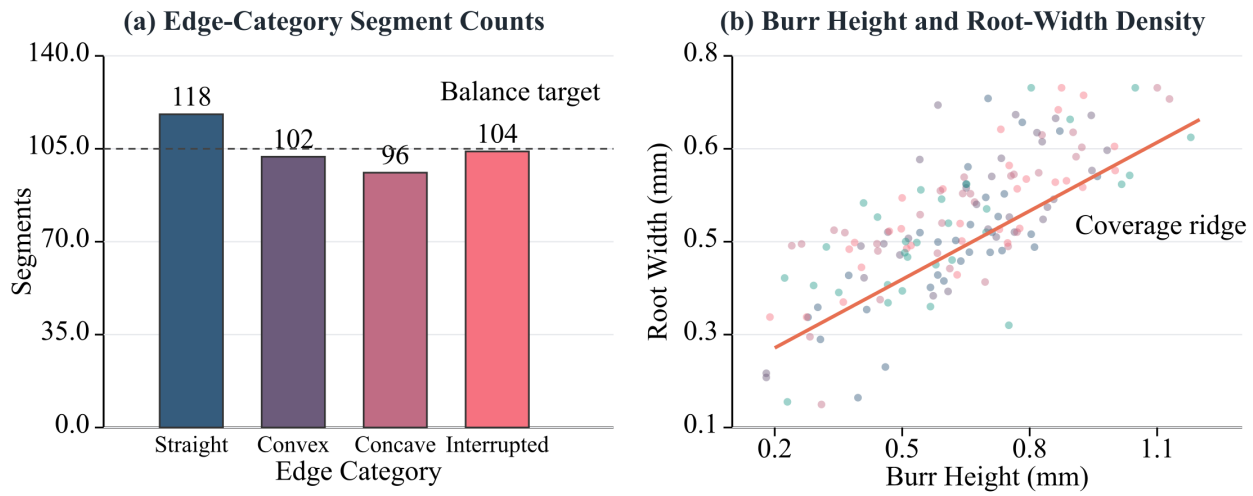


Figure 3. Dataset composition and geometric coverage: (a) edge-category segment counts; (b) burr-height and root-width density

The data acquisition plan varied feed speed from 40 to 140 mm/s and nominal normal force from 6 to 18 N. Every segment was measured before and after deburring using the same profile head, while selected samples were verified by an offline confocal profilometer. The offline measurements were used to audit the inline profile head on representative straight, curved, and interrupted edges rather than to replace the online measurement stream. The measurement protocol follows the view that robotic finishing data should report process variability rather than only average removal quality [25]. The six-dimensional force stream was synchronized with robot encoder data and trimmed into 0.64 s windows with 50% overlap. Figure 4(a) shows the normal-force distributions under the four nominal force levels; the 18 N condition approached the 20 N safety line in the upper whisker, which explains why force clipping was activated more frequently at the highest load. Figure 4(b) relates profile discontinuity score to peak force overshoot and shows a nonlinear rise after a discontinuity score of 0.65, where interrupted edges generated overshoot values above 5 N.

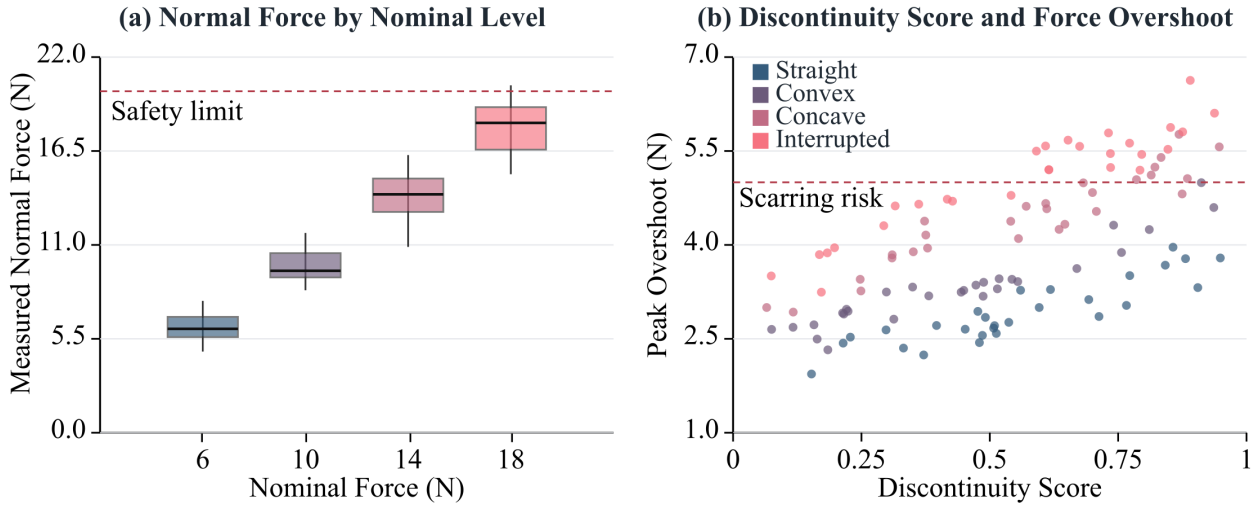


Figure 4. Force distribution and discontinuity response: (a) force-component distributions across nominal force levels; (b) peak overshoot against profile discontinuity score

The segment distribution was intentionally not perfectly uniform. Straight edges accounted for the largest group because they were needed for stable reference-force labeling, but convex, concave, and interrupted edges were kept close enough in count to prevent the model from treating difficult geometries as exceptions. Burr height was concentrated in the middle of the manufacturing range, yet the long tail above 1.0 mm created the high-load states needed to test bounded force compensation. Root width increased with burr height, but the density scatter was wide enough to include tall flexible burrs and short stiff burrs. That spread is technically important because those two cases may require opposite force corrections even if their initial height appears similar.

Force signals were inspected in the tool frame because a fixed sensor-frame threshold produced inconsistent behavior when the robot posture changed around curved contours. The transformed normal force was used as the main controlled variable, while tangential force and moments were used as explanatory channels for friction, leverage, and engagement depth. The force-distribution pattern indicates that nominal force alone does not determine contact severity, since

dispersion grows with higher force levels and becomes more exposed near the safety boundary. The discontinuity scatter provides a second view of the same issue: samples with similar discontinuity scores can still generate different overshoot values when edge category changes, which justifies feeding both profile morphology and six-dimensional wrench history to the controller.

4.2. Force-Control Accuracy and Surface Quality

Four controllers were compared: conventional PID admittance, an LSTM fusion network, a compact Transformer, and the proposed UniFormerV2 model. All controllers used the same robot path, initial burr distribution, sensing layout, and post-process measurement protocol; the learning baselines were evaluated on the same synchronized windows as the proposed model. Force peaks above a conservative process threshold are commonly treated as a warning sign in robotic edge finishing because they can precede scarring or chatter marks [26]. Under the complete test set, the proposed model achieved a normal-force RMSE of 1.18 N, compared with 2.74 N for PID admittance, 1.86 N for LSTM fusion, and 1.47 N for the compact Transformer. Figure 5(a) presents the RMSE and mean absolute error by controller; the gap between RMSE and MAE is largest for PID admittance, indicating that high-amplitude contact events dominate its error distribution. Figure 5(b) shows transient behavior on interrupted edges, where UniFormerV2 reduced peak overshoot from 6.1 N to 3.8 N and shortened settling time from 0.42 s to 0.24 s compared with PID admittance.

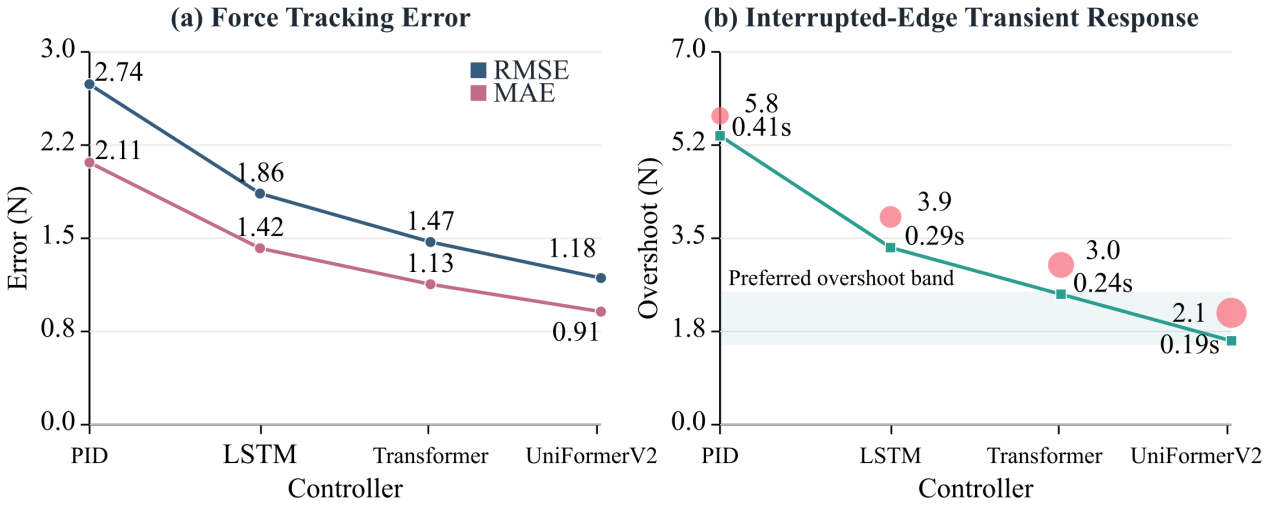


Figure 5. Controller accuracy and transient response: (a) force tracking errors across controllers; (b) overshoot and settling behavior on interrupted edges

The surface-quality measurements show that force accuracy translated into process improvement rather than only cleaner sensor traces. Roughness was measured along the deburred edge direction on the finished chamfer band, and selected measurements were cross-checked against the offline profilometer. Mean burr removal rate reached 96.4% for the proposed method, compared with 88.9% for PID admittance, 92.7% for LSTM fusion, and 94.1% for the compact Transformer. Prior work on adaptive finishing argues that geometric look-ahead is valuable when contact stiffness varies along the edge [27]. Figure 6(a) displays the roughness distribution by edge category; straight edges were finished to an average Ra of approximately 0.76 micrometer, while interrupted edges remained closer to 0.91 micrometer because the tool repeatedly entered and exited contact. Figure 6(b) plots residual burr height against commanded force correction and shows that corrections between 1.5 and 2.8 N corresponded to most samples below the 35 micrometer residual target. Figure 6(c) gives removal consistency over feed speed and nominal force, where the 100 mm/s and 12 N region produced the most stable results across repeated segments.

The ablation experiment separates the effect of force-only input, profile-only input, late fusion, and the proposed cross-stream UniFormerV2 fusion. Feature-attribution scores were averaged over held-out test segments and then checked separately on interrupted edges to verify that the ranking was not dominated by a single case. Multimodal ablation is required in learned manipulation systems because a lower prediction error does not necessarily imply a more stable physical action [28]. Figure 7(a) shows that force-only input achieved 1.62 N RMSE but produced a residual burr height of 43 micrometers on interrupted edges, while profile-only input reduced geometric misses but allowed unstable contact during convex segments. Figure 7(b) compares feature-attribution scores and indicates that normal force, moment about the tool tangent, burr height, and discontinuity score dominate the compensation decision. Figure 7(c) shows that a 60 ms look-ahead horizon achieved the best compromise between RMSE and removal rate; shorter horizons missed upcoming interruptions, while longer horizons included geometry that was too far from the current contact state.

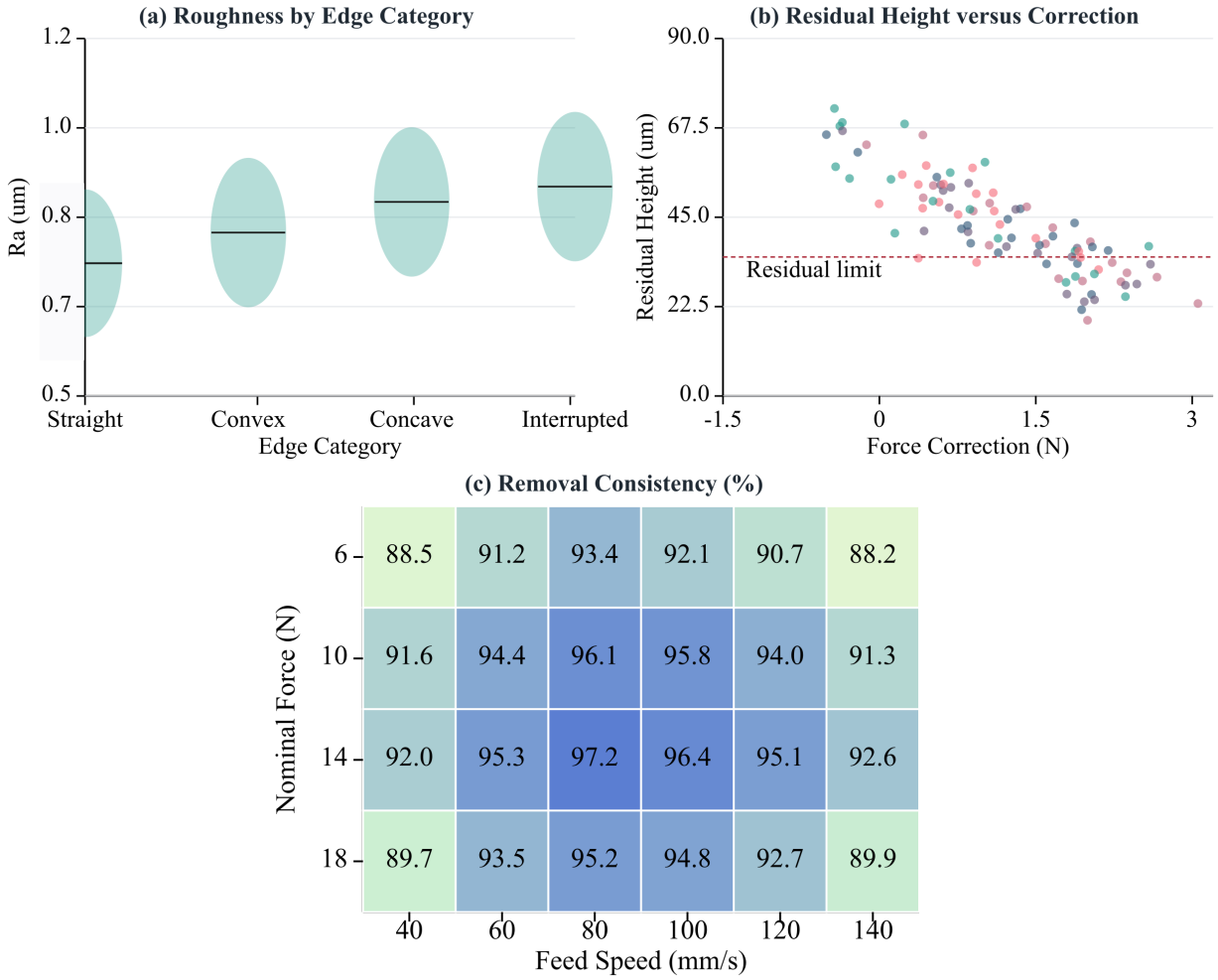


Figure 6. Surface quality and process consistency: (a) post-process roughness by edge category; (b) residual burr height versus force correction; (c) removal consistency over feed speed and nominal force

The difference between RMSE and MAE further reveals how each controller handled rare contact peaks. PID admittance had a large separation between the two metrics, while LSTM fusion narrowed that gap but delayed its response when the force transient rose faster than the recurrent hidden state adapted. The compact Transformer improved peak handling, yet its attention weights were less stable when the incoming profile contained discontinuities and the previous force window remained quiet. UniFormerV2 produced the smallest separation because its local branch reacted to the force impulse while the profile branch prepared the correction before the measured peak reached its maximum. The transient curve shows that the command settled without a long undershoot after the first impact, which is critical for maintaining cutting continuity on interrupted contours.

The surface-quality figure gives a more detailed view of how control behavior appears on the workpiece. The roughness distribution shows that the proposed method did not eliminate the category effect, but it compressed the roughness range compared with the baseline controllers. The residual-height scatter shows that samples with negative or weak correction frequently remain above the 35-micrometer residual limit, whereas moderate positive correction pulls most points below the limit. The consistency heat map shows acceptable removal at low feed but weaker roughness stability because the tool spends more time rubbing the edge, while the high-feed region loses consistency because tall burr roots cannot always be removed in one pass. These interactions indicate that the model does not simply increase force; it adjusts force according to the local profile and the recent wrench response.

The ablation plots also indicate how the two sensing streams divide their roles. The variant comparison shows that force-only input recognizes impacts but cannot distinguish whether the impact is caused by burr fracture or an approaching edge break. The attribution profile assigns large weight to normal force, burr height, tangent moment, and discontinuity score, which is mechanically plausible because these variables correspond to load demand, geometry, off-center engagement, and impact-prone edge shape. The horizon-sensitivity curve shows that a 60 ms look-ahead horizon gives the best balance between early preparation and profile uncertainty. A longer horizon slightly reduces reliability because the future profile becomes less aligned with the exact tool contact point under feed-rate perturbation.

4.3. Robustness, Latency, and Process Interpretation

Robustness was evaluated by adding profile noise, force bias, and feed-rate perturbations not present in the training set. The selected noise and bias ranges represent common inline sensing degradation, including edge shadowing, reflective aluminum surfaces, sensor remounting, and imperfect tool-frame transformation. Industrial robot controllers are expected to tolerate sensing drift and calibration error rather than operate only under laboratory-aligned measurements [29]. Figure 8(a) reports the sensitivity curve under profile noise from 0 to 0.16 mm, where UniFormerV2 kept removal rate above 93.1% at the highest noise level while the compact Transformer decreased to 90.4%. Figure 8(b) shows that a force bias of 1.5 N increased UniFormerV2 RMSE by 0.24 N, compared with 0.51 N for the LSTM model. Figure 8(c) compares latency and memory footprint; the proposed model required 8.7 ms inference time and 46 MB of parameters. Real-time learning components in industrial control must be evaluated against the available control-cycle budget, not only against offline accuracy [30].

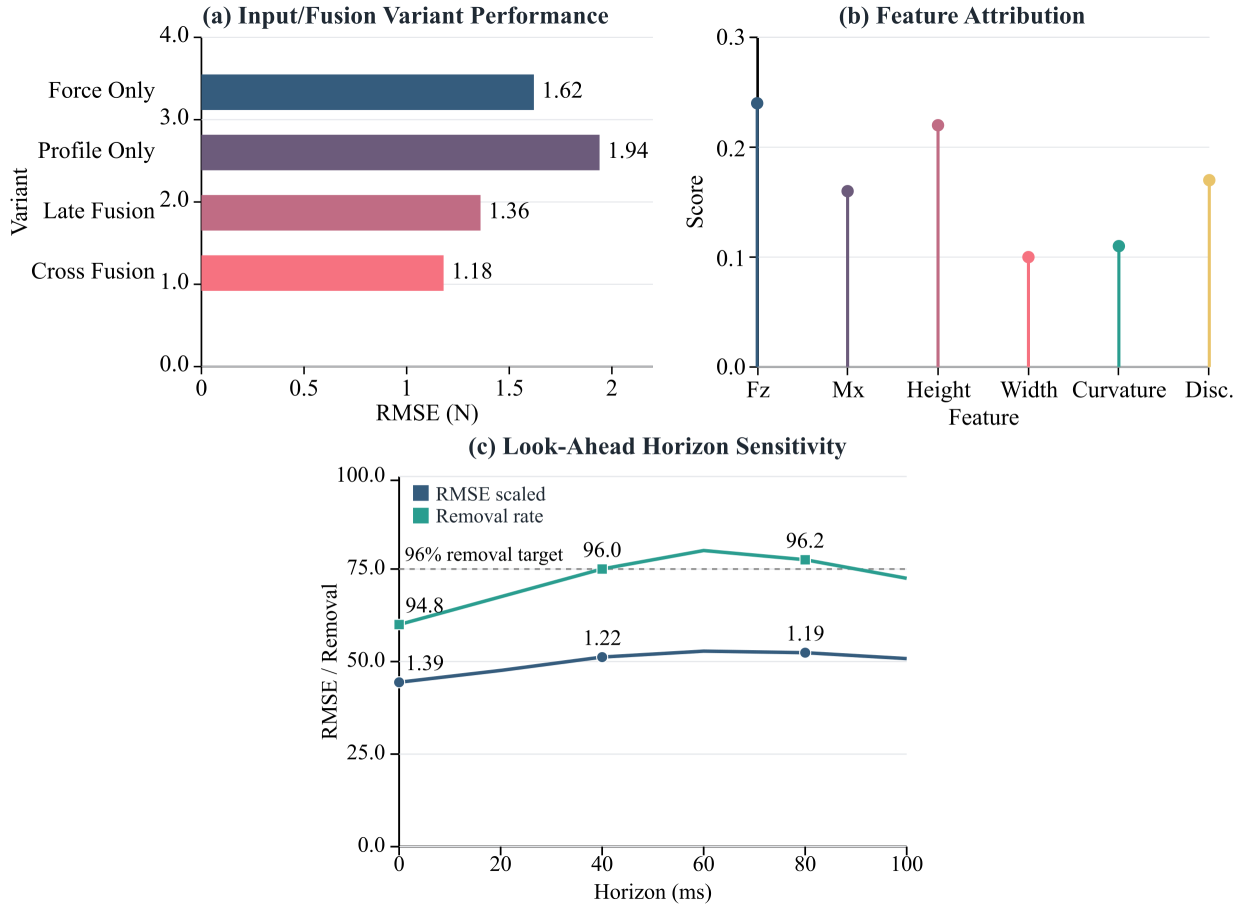


Figure 7. Ablation analysis: (a) input/fusion variant performance; (b) feature-attribution scores; (c) look-ahead horizon sensitivity

The process interpretation analysis examined whether the model responded to physically meaningful contact changes. Contact interpretation is relevant for deployable learning controllers because engineers need evidence that model actions correspond to measurable process states [31]. During straight-edge segments with moderate burr height, the correction stayed within +/-1.8 N and mainly damped short force impulses. Figure 9(a) presents a time-aligned interrupted-edge case where the commanded force correction rose from 0.4 N to 2.6 N before the measured normal-force peak. Figure 9(b) compares the residual profile before and after deburring along the same edge, where the peak burr height was reduced below the 35-micrometer limit along most of the inspected coordinate. Figure 9(c) maps the local relation between burr height, tangential force, and removal quality, with the most stable removal appearing near moderate burr height and tangential force between roughly 4.5 and 5.8 N.

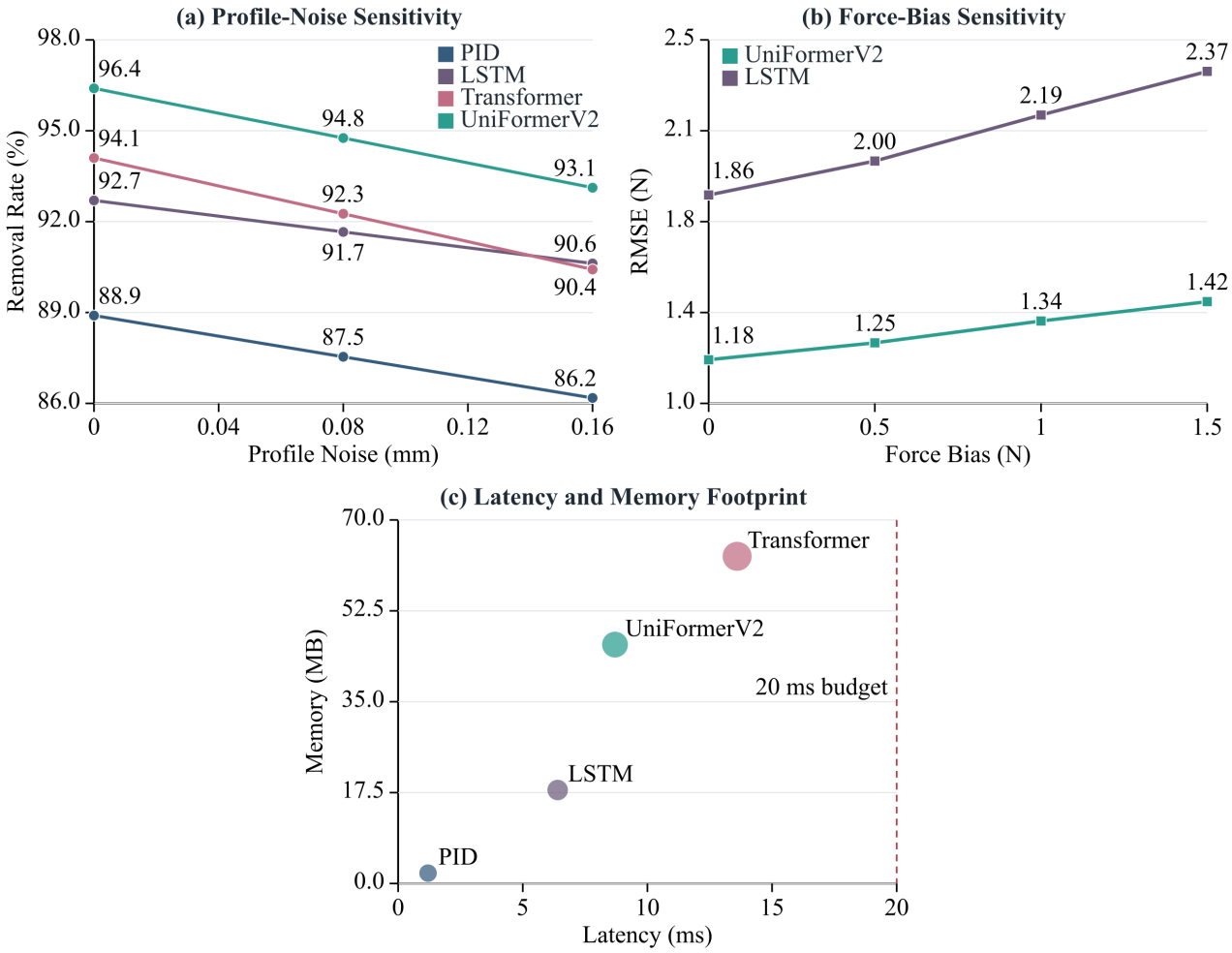


Figure 8. Robustness and deployment cost: (a) removal-rate sensitivity to profile noise; (b) force-bias sensitivity; (c) latency and memory footprint

Controlled comparison requires the same tool, robot path, sensing layout, and initial burr distribution when controller performance is being attributed to the algorithm rather than to fixture or path variation [32]. Table 1 provides the numerical comparison used for the main evaluation. Repeated-segment variability was retained in the analysis so that the table values represent process behavior over changing burr geometry rather than a single favorable pass. UniFormerV2 reached the lowest force RMSE, the highest burr removal rate, the lowest post-process roughness, and the shortest settling time among the learned and non-learned methods. The compact Transformer approached its surface-quality level but required 13.6 ms inference time and showed a larger overshoot on interrupted edges. PID admittance remained stable in simple straight-edge trials but was less capable of absorbing abrupt discontinuities because it had no geometric look-ahead.

Table 1. Quantitative comparison of force-control and deburring-quality indicators

Controller	Force RMSE (*N*)	Overshoot (*N*)	Settling Time (*s*)	Removal Rate (*%*)	Post Ra (*um*)	Latency (*ms*)
PID Admittance	2.74	5.8	0.41	88.9	1.34	1.2
LSTM Fusion	1.86	3.9	0.29	92.7	1.05	6.4
Compact Transformer	1.47	3.0	0.24	94.1	0.93	13.6
UniFormerV2	1.18	2.1	0.19	96.4	0.81	8.7

Robustness to profile noise is a meaningful test because inline surface sensing in deburring is rarely clean. Chips, tool vibration, changing reflectance, and edge shadowing can all distort the measured ridge. The proposed model degraded gradually rather than abruptly because the profile confidence feature allowed the fusion layer to reduce trust in uncertain geometric evidence. At 0.08 mm added noise, UniFormerV2 retained a removal rate near 94.8%, while the compact Transformer and LSTM baselines showed larger drops. The PID controller was less sensitive to profile noise

because it did not use profile information, but its baseline removal rate was already lower. This contrast separates robustness from absolute finishing quality and shows why both curves must be read together.

The force-bias test simulates zero drift, imperfect tool-frame transformation, and small calibration shifts after sensor remounting. A 1.5 N bias is severe for a process whose useful correction range is only a few newtons. Under the bias curve, the LSTM model accumulated the bias in its hidden state and produced delayed corrections after several windows. UniFormerV2 was less affected because the profile stream supplied an independent expectation of upcoming load, and the bounded output prevented the bias from becoming a large command jump. In the deployment-cost plot, the measured latency leaves approximately 11 ms for sensor preprocessing, safety checks, and communication inside the 20 ms outer-loop budget. The model size of 46 MB is practical for an industrial GPU and could be reduced further through quantization if the controller is moved to an embedded edge device.

The case-level interpretation in the final data figure clarifies how the model behaves within a single contact event. In the time-aligned contact curve, the surface profile branch raises the correction before the interrupted edge break, while the force branch dampens the command after the normal-force peak begins to rise. In the residual-profile trace, the shoulder near the entry side of the interruption remains visible even though the dominant burr peak is removed, indicating that abrupt geometric transitions still challenge single-pass finishing. In the local quality map, large markers cluster around the moderate-load region, whereas high burr height combined with excessive tangential force produces lower removal quality. Supervisory structures are often used around learned controllers in contact tasks to keep learned corrections inside validated mechanical and safety envelopes [33].

The failure-case inspection identified two remaining weaknesses. First, highly reflective profile regions near freshly cut chamfers caused short reductions in profile confidence, and those events increased residual burr height by 11 to 18 micrometers in isolated cases. Second, tool wear after 240 m of accumulated cutting shifted the tangential force baseline and reduced the reliability of moment-based attribution. These observations indicate that future deployment should couple profile confidence monitoring with tool-state adaptation and feed-speed-aware look-ahead calibration.

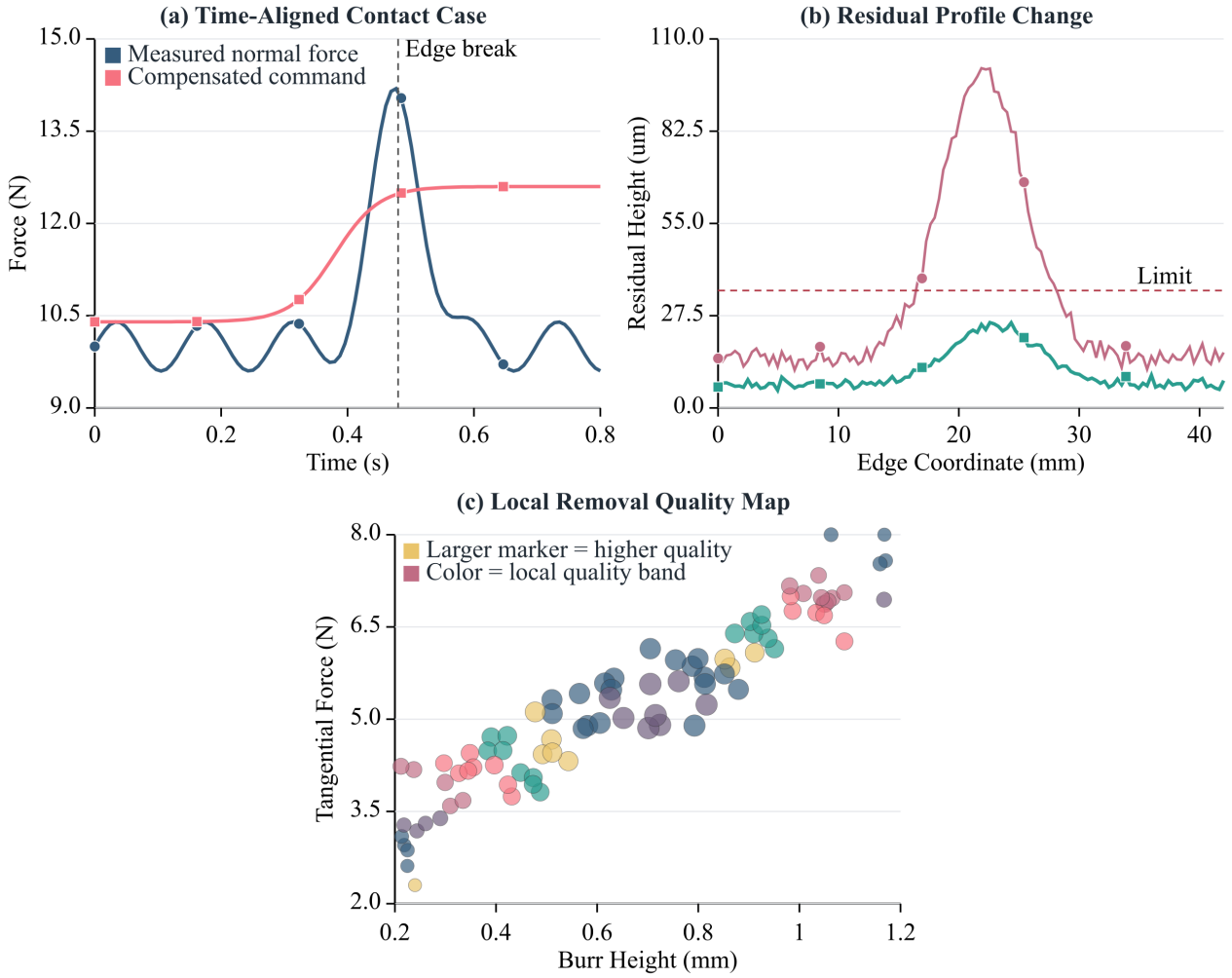


Figure 9. Case-level interpretation: (a) time-aligned force correction and measured normal force; (b) residual profile before and after deburring; (c) local relation among burr height, tangential force, and removal quality

5. Conclusion

This paper presented a UniFormerV2-based force-control model for robotic deburring with synchronized six-dimensional force and surface profile data streams. The method uses local force-token mixing, profile-aware global relation modeling, cross-stream fusion, and bounded force-command compensation inside an admittance-control structure. The manuscript established the sensing architecture, model formulation, training objective, deployment logic, and engineering evaluation framework needed for contact-sensitive edge finishing.

The present study still has limitations. The experimental materials and tools were limited to aluminum alloy workpieces and a rotary-file deburring process. The profile sensor was mounted in a fixed look-ahead configuration, which may not be optimal for narrow cavities, reflective surfaces, or complex free-form components. The fixed look-ahead distance may also interact with feed speed because the same spatial offset corresponds to different prediction horizons at different path velocities. The model also requires representative edge-segment data before deployment, and its behavior under severe tool wear, coolant spray, or multi-pass finishing remains to be evaluated.

Future work will extend the model toward online tool-state adaptation, richer three-dimensional edge reconstruction, and transfer learning across materials and tool geometries. Another important direction is the integration of uncertainty estimation into the force-compensation output so that the robot can adjust speed, request remeasurement, or switch to a conservative control mode when sensing confidence decreases. These extensions would make learning-assisted deburring more practical for flexible manufacturing cells.

6. Declarations

6.1 Author Contributions

Waldemar Brzozowski contributes to conceptualization, methodology, software, validation, analysis, investigation, data collection, draft preparation, manuscript editing, visualization, supervision, project administration, and funding acquisition. Bronisław Kaczor contributes to validation, analysis, investigation, data collection, draft preparation. Arkadiusz Sadowski contributes to software, validation, analysis, investigation. All authors have read and agreed with the manuscript before its submission and publication.

6.2 Funding and Acknowledgments

This research received no specific financial support from any funding agency.

6.3 Institutional Review Board Statement

Not applicable.

6.4 Informed Consent Statement

Not applicable.

6.5 Declaration of Competing Interest

Not applicable.

6.6 Declaration of Competing Interest

The authors declare that they have no known competing financial interests or personal relationships that could have appeared to influence the work reported in this paper.

6.7 Declaration of generative AI and AI-assisted technologies

During the preparation of this manuscript, the authors utilized Grammarly for linguistic polishing, logical organization and draft revision. The generative AI tool was not involved in research design, data collection, data analysis, or the equation of core conclusions. All outputs generated by AI were reviewed, revised and verified manually by the authors. The authors take full responsibility for all content of this manuscript.

7. References

[1] Li, J., Guan, Y., Chen, H., Wang, B., Zhang, T., Liu, X., ... & Zhang, H. (2020). A high-bandwidth end-effector with active force control for robotic polishing. IEEE Access, 8, 169122-169135. https://doi.org/10.1109/access.2020.3022930

[2] Wu, X., Huang, Z., Wan, Y., Liu, H., & Chen, X. (2020). A novel force-controlled spherical polishing tool combined with self-rotation and co-rotation motion. IEEE Access, 8, 108191-108200. https://doi.org/10.1109/access.2020.2997968

[3] Ma, K., Han, L., Sun, X., Liang, C., Zhang, S., Shi, Y., & Wang, X. (2020). A path planning method of robotic belt grinding for workpieces with complex surfaces. IEEE/ASME Transactions on Mechatronics, 25(2), 728-738. https://doi.org/10.1109/tmech.2020.2974925

[4] Guo, W., Zhu, Y., & He, X. (2020). A robotic grinding motion planning methodology for a novel automatic seam bead grinding robot manipulator. IEEE Access, 8, 75288-75302. https://doi.org/10.1109/access.2020.2987807

[5] Ren, X., Chai, Z., Xu, J., Zhang, X., He, Y., Chen, H., & Chen, X. (2020). A new method to achieve dynamic heat input monitoring in robotic belt grinding of Inconel 718. Journal of Manufacturing Processes, 57, 575-588. https://doi.org/10.1016/j.jmapro.2020.07.018

[6] Xie, H. L., Li, J. R., Liao, Z. Y., Wang, Q. H., & Zhou, X. F. (2020). A robotic belt grinding approach based on easy-to-grind region partitioning. Journal of Manufacturing Processes, 56, 830-844. https://doi.org/10.1016/j.jmapro.2020.03.051

[7] Dong, Y., Ren, T., Hu, K., Wu, D., & Chen, K. (2020). Contact force detection and control for robotic polishing based on joint torque sensors. The International Journal of Advanced Manufacturing Technology, 107(5-6), 2745-2756. https://doi.org/10.1007/s00170-020-05162-8

[8] Xiao, M., Ding, Y., Fang, Z., & Yang, G. (2020). Contact force modeling and analysis for robotic tilted-disc polishing of freeform workpieces. Precision Engineering, 66, 188-200. https://doi.org/10.1016/j.precisioneng.2020.04.019

[9] Zhang, H., Li, L., Zhao, J., Zhao, J., Liu, S., & Wu, J. (2020). Design and implementation of hybrid force/position control for robot automation grinding aviation blade based on fuzzy PID. The International Journal of Advanced Manufacturing Technology, 107(3-4), 1741-1754. https://doi.org/10.1007/s00170-020-05061-y

[10] Mesmer, P., Neubauer, M., Lechler, A., & Verl, A. (2020). Drive-based vibration damping control for robot machining. IEEE Robotics and Automation Letters, 5(2), 564-571. https://doi.org/10.1109/lra.2019.2960723

[11] Xiao, M., Ding, Y., & Yang, G. (2022). A model-based trajectory planning method for robotic polishing of complex surfaces. IEEE Transactions on Automation Science and Engineering, 19(4), 2890-2903. https://doi.org/10.1109/tase.2021.3095061

[12] Lv, C., Zou, L., Huang, Y., Li, H., Wang, T., & Mu, Y. (2022). A novel toolpath for robotic adaptive grinding of extremely thin blade edge based on dwell time model. IEEE/ASME Transactions on Mechatronics, 27(6), 4429-4439. https://doi.org/10.1109/tmech.2022.3156804

[13] Chang, G., Pan, R., Xie, Y., Yang, J., Yang, Y., & Li, J. (2022). Research on constant force polishing method of curved mold based on position adaptive impedance control. The International Journal of Advanced Manufacturing Technology, 122(2), 697-709. https://doi.org/10.1007/s00170-022-09943-1

[14] Wang, Z., Zou, L., Luo, G., Lv, C., & Huang, Y. (2022). A novel selected force controlling method for improving robotic grinding accuracy of complex curved blade. ISA Transactions, 129, 642-658. https://doi.org/10.1016/j.isatra.2021.12.032

[15] Feng, H., Ren, X., Li, L., Zhang, X., Chen, H., Chai, Z., & Chen, X. (2021). A novel feature-guided trajectory generation method based on point cloud for robotic grinding of freeform welds. The International Journal of Advanced Manufacturing Technology, 115(5-6), 1763-1781. https://doi.org/10.1007/s00170-021-07095-2

[16] Li, L., Ren, X., Feng, H., Chen, H., & Chen, X. (2021). A novel material removal rate model based on single grain force for robotic belt grinding. Journal of Manufacturing Processes, 68, 1-12. https://doi.org/10.1016/j.jmapro.2021.05.029

[17] Lakshminarayanan, S., Kana, S., Mohan, D. M., Manyar, O. M., Then, D., & Campolo, D. (2021). An adaptive framework for robotic polishing based on impedance control. The International Journal of Advanced Manufacturing Technology, 112(1-2), 401-417. https://doi.org/10.1007/s00170-020-06270-1

[18] Wang, T., Zou, L., Wan, Q., Zhang, X., Li, Y., & Huang, Y. (2021). A high-precision prediction model of surface roughness in abrasive belt flexible grinding of aero-engine blade. Journal of Manufacturing Processes, 66, 364-375. https://doi.org/10.1016/j.jmapro.2021.04.002

[19] Wang, N., Zhang, G., Ren, L., Pang, W., & Wang, Y. (2021). Vision and sound fusion-based material removal rate monitoring for abrasive belt grinding using improved LightGBM algorithm. Journal of Manufacturing Processes, 66, 281-292. https://doi.org/10.1016/j.jmapro.2021.04.014

[20] Xie, H., Li, W. L., Jiang, C., Zhu, D. H., Yin, Z. P., & Ding, H. (2021). Pose error estimation using a cylinder in scanner-based robotic belt grinding. IEEE/ASME Transactions on Mechatronics, 26(1), 515-526. https://doi.org/10.1109/tmech.2020.3038237

[21] Xiao, M., Zhang, T., Zou, Y., & Chen, S. (2021). Robotic constant force grinding control based on grinding model and iterative algorithm. Industrial Robot: the international journal of robotics research and application, 48(2), 270-279. https://doi.org/10.1108/ir-08-2020-0166

[22] Wang, Z., Zou, L., Duan, L., Liu, X., Lv, C., Gong, M., & Huang, Y. (2021). Study on passive compliance control in robotic belt grinding of nickel-based superalloy blade. Journal of Manufacturing Processes, 68, 168-179.

https://doi.org/10.1016/j.jmapro.2021.07.020

[23] Miller, G., Irani, R. A., & Ahmadi, M. (2021). The application of mechanistic cutting force models for robotic deburring. The International Journal of Advanced Manufacturing Technology, 115(1-2), 199-212. https://doi.org/10.1007/s00170-021-07070-x

[24] Zhang, H., Li, L., Zhao, J., & Zhao, J. (2021). The hybrid force/position anti-disturbance control strategy for robot abrasive belt grinding of aviation blade base on fuzzy PID control. The International Journal of Advanced Manufacturing Technology, 114(11-12), 3645-3656. https://doi.org/10.1007/s00170-021-07122-2

[25] Yang, J., Chen, H., Qi, R., Ding, H., & Yin, Y. (2023). A novel approach to robotic grinding guaranteeing profile accuracy using rigid-flexible coupling force control for free-formed surfaces. CIRP Annals, 72(1), 313-316. https://doi.org/10.1016/j.cirp.2023.04.069

[26] Mu, Y., Wang, Z., Zou, L., Wang, W., Lv, C., & Wang, A. (2023). A novel regional force control strategy based on seven-axis linkage grinding system to improve blade machining accuracy. Journal of Manufacturing Processes, 97, 235-247. https://doi.org/10.1016/j.jmapro.2023.05.005

[27] Ren, X., Huang, X., Gao, K., Xu, L., Li, L., Feng, H., Zhang, X., Chen, H., Chai, Z., & Chen, X. (2023). A review of recent advances in robotic belt grinding of superalloys. The International Journal of Advanced Manufacturing Technology, 127(3-4), 1447-1482. https://doi.org/10.1007/s00170-023-11574-z

[28] Liang, X., Cai, Z., Zeng, C., Mu, Z., Li, Z., Yang, F., Chen, T., Dong, S., Deng, C., & Niu, S. (2023). A robotic polishing trajectory planning method for TBCs of aero-engine turbine blade using measured point cloud. Industrial Robot: the international journal of robotics research and application, 50(2), 275-286. https://doi.org/10.1108/ir-05-2022-0141

[29] Chen, C., Cai, Z., Chen, T., Li, Z., Yang, F., & Liang, X. (2023). A vision-based calibration method for aero-engine blade-robotic grinding system. The International Journal of Advanced Manufacturing Technology, 125(5-6), 2195-2209. https://doi.org/10.1007/s00170-023-10822-6

[30] Huang, Y., Liu, G., Xiao, G., & Xu, J. (2023). Abrasive belt grinding force and its influence on surface integrity. Materials and Manufacturing Processes, 38(7), 888-897. https://doi.org/10.1080/10426914.2022.2116042

[31] Xie, H., Wang, Q., Ong, S. K., Nee, A. Y. C., Zhou, X., & Liao, Z. (2023). Automatic generation of interference-free and posture-smooth toolpath for robotic belt grinding of complex workpieces. IEEE/ASME Transactions on Mechatronics, 28(1), 518-530. https://doi.org/10.1109/tmech.2022.3205852

[32] Zheng, H., Liang, C., Gao, F., & Qi, C. (2023). Automatic surface polishing based on probe measurement and force-position decoupling control. The International Journal of Advanced Manufacturing Technology, 129(5-6), 2429-2442. https://doi.org/10.1007/s00170-023-12447-1

[33] Huang, X., Guo, Y., Guo, W., Qi, B., Ren, X., Chai, Z., & Chen, X. (2023). Comprehensive investigations into the force and thermal characteristics of belt grinding Inconel 718 under constant normal forces. Journal of Manufacturing Processes, 99, 78-95. https://doi.org/10.1016/j.jmapro.2023.04.082